Desalination 586 (2024) 117853

Contents lists available at ScienceDirect

Desalination

journal homepage: www.elsevier.com/locate/desal

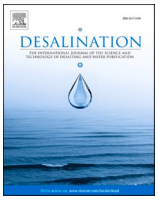

Cathodic precipitation of calcium carbonate and its impact on the electrosorption of sodium in flow-through capacitive deionization

Yazeed Algurainy [a,b], Douglas F. Call [a,*]

[a] Department of Civil, Construction, and Environmental Engineering, North Carolina State University, Campus Box, 7908, Raleigh, USA
[b] Department of Civil Engineering, King Saud University, Campus Box 2454, Riyadh, Kingdom of Saudi Arabia

HIGHLIGHTS

- Calcium carbonate precipitated on the cathode in flow-through capacitive deionization
- Precipitation reduced sodium adsorption capacity by almost 70 %
- Cathode micropore volume decreased by 30 % after precipitation
- Precipitation was associated with an increase in resistance and decrease in capacitance

GRAPHICAL ABSTRACT

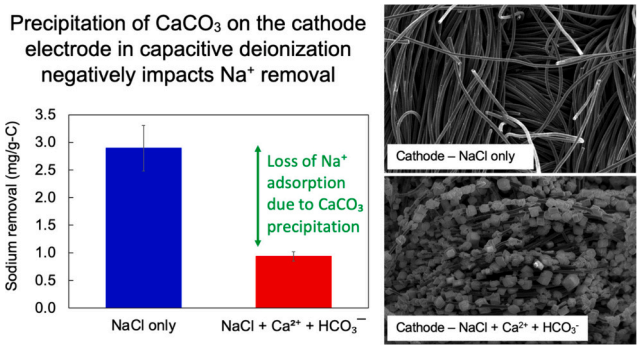

ARTICLE INFO

Keywords:
Desalination
Capacitive deionization
Porous electrodes
Precipitation

ABSTRACT

Capacitive deionization (CDI) is an electrochemical desalination technology that removes ions from brackish water through electrosorption within charged porous electrodes. Brackish waters contain ions that may form precipitates on the electrodes (e.g., Ca^{2+}, Mg^{2+}, CO_3^{2-}), especially in response to localized pH increases common at cathodes. Here we study the formation of calcium carbonate ($CaCO_{3(s)}$) on the cathode and its effect on Na^+ removal using defined solution chemistries. We found that $CaCO_{3(s)}$ formed during the charging phase at the cathode, but not the anode. Local precipitation was likely due to the in situ basic pH caused by the reduction of dissolved oxygen at the cathode. The deposition of solids reduced Na^+ adsorption capacity by 67 % (0.94 ± 0.08 mg/g-C) compared to a control where no Ca^{2+} and HCO_3^- were present. We attributed this reduction primarily to the ~30 % decrease in micropores available for electrosorption. These interior pores were blocked by non-porous $CaCO_3$ crystals. Cathodes with precipitation had reduced capacitance and increased resistance. The deposition of non-conductive crystals hindered the transfer of charge and restricted the movement of ions from the bulk solution toward the electrode surface and also through the pores' structure. Since precipitation was found to be detrimental to salt removal, future research is needed to reduce scaling and/or strategies to regenerate the electrosorption capacity of electrodes. For other applications, such as water softening, research to improve precipitation might be desired.

* Corresponding author.
E-mail address: dfcall@ncsu.edu (D.F. Call).

https://doi.org/10.1016/j.desal.2024.117853
Received 25 March 2024; Received in revised form 10 June 2024; Accepted 15 June 2024
Available online 18 June 2024

1. Introduction

Capacitive deionization (CDI) is an emerging technology for brackish water desalination. In CDI, a pair of porous electrodes, commonly made of activated carbon (AC), is charged using low voltages (< 1.2 V). Charged ions from the feedwater are electrosorbed (removed) by the electrode of opposite charge (charging phase). The adsorbed species are then released back into the water and collected as a brine when the electrodes are short-circuited or their polarity/current reversed (discharging phase) [1–3]. CDI research, including the development of new electrode materials and cell architectures, fundamental understanding of capacitive and faradaic processes, and strategies to extend cell stability, has advanced substantially over the past few decades [4–9]. A limitation underpinning many of the advancements made is the use of single monovalent salts (most commonly NaCl) to mimic the salinity of real waters. To evaluate the feasibility for brackish water desalination, understanding ion removal in more complex matrices is critical [10,11].

The inorganic composition of real brackish waters is complex and may lead to undesirable reactions, including precipitation. Brackish groundwater may contain, beside Na^+ and Cl^-, high concentrations of Ca^{2+}, Mg^{2+}, CO_3^{2-}, and SO_4^{2-} (**Table S1**). In single salt experiments, electrosorption of these ions is commonly reported or assumed as the main mechanism of removal [12–14]. For example, removal of Ca^{2+} and Mg^{2+} occurred in synthetic solutions containing CO_3^{2-} [2–15–17], but the mechanism(s) was(were) not reported. Understanding the mechanism(s) of ions removal is important because of the potential for certain brackish water ions to form precipitates naturally or through electrochemically-driven processes, which could result in pore blocking, reduced electrode capacitance, and increased resistance. This in turn can lead to a severe decline in desalination performance. Precipitation of solids on electrodes in electrochemical cells other than CDI is well-documented and is promoted by electrode-driven pH changes [18–20]. When pH increases at a cathode, the thermodynamic favorability of precipitation improves for many reactions. One example is the precipitation of hydroxyapatite ($Ca_{10}(PO_4)_6(OH)_2$) on titanium electrodes driven by large voltages (> 1.5 V) that electrolyze water and increase cathodic pH [1,18]. In CDI, despite using lower voltages, strong pH variations have been measured in CDI effluents, especially in flow-through CDI (FT-CDI) cells [21–23]. At the cathode, dissolved oxygen can be reduced to OH^- and H_2O_2, resulting in high local pH values. For example, Holubowitch et al. [23] reported a pH of 11.5 near the cathode in non-buffered solutions. In brackish groundwater containing Ca^{2+} and Mg^{2+}, basic pH near the cathode and migration of cations toward the cathode due to the applied electric field may provide favorable conditions for precipitation of a variety of solids (Eqs. 1–5) [24].

$$Ca^{2+} + CO_3^{2-} \Leftrightarrow CaCO_{3(s)} \quad K_{sp} = 10^{-8.48} \tag{1}$$

$$Ca^{2+} + SO_4^{2-} \Leftrightarrow CaSO_{4(s)} \quad K_{sp} = 10^{-4.61} \tag{2}$$

$$Ca^{2+} + Mg^{2+} + 2CO_3^{2-} \Leftrightarrow CaMg(CO_3)_{2(s)} \quad K_{sp} = 10^{-17.09} \tag{3}$$

$$Mg^{2+} + 2OH^- \Leftrightarrow Mg(OH)_{2(s)} \quad K_{sp} = 10^{-11.25} \tag{4}$$

$$3Mg^{2+} + Ca^{2+} + 4CO_3^{2-} \Leftrightarrow Mg_3Ca(CO_3)_{4(s)} \quad K_{sp} = 10^{-29.97} \tag{5}$$

Solid formation on the cathode may impact the accessibility of cations (e.g., Na^+) to adsorption sites within the pores. In turn, desalination via electrosorption may decrease. Anecdotal evidence for precipitation exists in studies using real waters, but a comprehensive fundamental investigation of precipitation and its impact on desalination using porous electrodes is still lacking [25–28].

Our objectives were to investigate the potential for electrochemically driven precipitation on the cathode and determine its influence on electrode properties and Na^+ adsorption in FT-CDI. We used a defined solution chemistry containing Ca^{2+} and HCO_3^- to study $CaCO_{3(s)}$ precipitation as a model reaction. We chose this reaction because of the abundance of these two ions in typical brackish groundwater (**Table S1**) and the favorable thermodynamics for $CaCO_{3(s)}$ precipitation under elevated pH. To visualize precipitates on the electrodes, we used scanning electron microscopy (SEM). The impacts of deposits on the physical and electrochemical properties of the cathode were quantified by monitoring changes in N_2 sorption (to determine the pore size distribution of the electrode), and cyclic voltammetry (CV; electrode capacitance), as well as electrochemical impedance spectroscopy (EIS; resistance characterization), respectively. We coupled those tests with total salt and cation concentration measurements during charging and discharging to assess precipitation and evaluate its impact on the Na^+ adsorption capacity of the cathode. Our results show that the precipitation of $CaCO_{3(s)}$ reduced the total volume of cathode micropores, decreased the capacitance, and increased the resistance, which in turn decreased Na^+ adsorption.

2. Methods

2.1. Experimental setup and operation

Commercially-available activated carbon cloth (ACC) (ACC-5092-15, Nippon Kynol, Japan) was used without chemical pre-treatment. Many properties of this material are available in Kim et al. (2017) (**Table S2**) [29]. To remove dust and impurities before use, the ACC was washed with deionized (DI) water (18.2 μΩ, Dracor Water System), dried in air at 105°C for 3 h, and stored in a desiccator. The FT-CDI cell was identical to a previously described design [21]. We chose to place the cathode in the upstream orientation to mimic pH conditions most favorable for precipitation at the cathode. When the cathode is positioned downstream of the anode, acidity from anodic reactions (e.g., carbon oxidation) decreases the pH contacting the cathode [21,22,30–32]. The feedwater was continuously pumped through the cell at 3 mL/min and collected at the effluent for further analysis. The CDI operation consisted of a charging phase at 1.2 V for 30 min and a discharging phase at 0 V for another 30 min over a total of 15 cycles (each cycle lasted 1 h). We did not test >15 cycles because we wanted to minimize the effects of anode oxidation, which become more pronounced in long-term tests, on our whole-cell analyses described below [30]. A potentiostat (VMP3, BioLogic, France) was used to control the applied voltages. The CDI cell was first operated without a voltage [open circuit voltage (OCV)] and flushed with DI water overnight to ensure influent and effluent pH were identical [33]. Then the influent was switched to one of the defined feedwater solutions for 24 h to reach a pseudo-equilibrium state with respect to non-electrosorption of ions [1,33,34]. To reduce the effects of electrode degradation over time and irreversible ion adsorption, new ACC electrodes were used for each experiment.

Synthetic solutions containing one or more salts to provide Na^+, Ca^{2+}, Cl^-, and/or HCO_3^- were tested. The solutions were prepared using NaCl (>99 % pure, Sigma Aldrich, USA), $CaCl_2$ (>99 % pure, Sigma Aldrich, USA) and $NaHCO_3$ (Laboratory grade, Ward's Science, USA). The concentrations tested were selected to meet two criteria: (1) fall within the range of concentrations in typical brackish groundwater (**Table S1**), and (2) result in an influent ionic strength that is common in CDI studies (< 3000 μS/cm) [3,10,35,36]. Solution 1 (Table 1) contained only NaCl and served as a positive control that established baseline removal of Na^+ in the absence of precipitation. In Solution 2, we added 2.5 mM $CaCl_2$ to Solution 1 to determine the impact of cation competition at the cathode (cation selectively) in the absence of precipitation. In Solution 3, we added 5 mM HCO_3^- to Solution 2 to provide conditions favorable for precipitation of $CaCO_3$. Including Na^+ in Solution 3 allowed us to determine the influence of precipitation on its removal. We used the following notation for each solution in our figures: Solution 1: NaCl = "Na^+", Solution 2: NaCl + $CaCl_2$ = "$Na^+ + Ca^{2+}$", and Solution 3: NaCl + $CaCl_2$ + $NaHCO_3$ = "$Na^+ + Ca^{2+} + HCO_3^-$"

2.2. Electrode characterization

Scanning electron microscopy (SEM; COXEM Scanning Electron Microscope EM-30 N instrument operated at 9 kV) images of pre- and post-experiment electrodes were obtained to visualize the morphology of the electrodes and evaluate for precipitate formation on the electrode surface. The SEM instrument was equipped with X-ray energy dispersive spectroscopy (EDS; Oxford Instruments AZtec software operated at 10 kV accelerating voltage) for elemental mapping. For the post-experiment electrodes, the samples were dried in air at 105 °C for 24 h after disassembling the cell. To avoid removing or dissolving surface-attached precipitates, the electrodes were not rinsed with DI water before drying.

Nitrogen gas sorption analysis was performed on the electrodes to characterize the pore size distribution using a Quantachrome Autosorb iQ Instrument. The samples were degassed in vacuum at 300 °C for 5.2 h before the analysis was carried out in liquid nitrogen at 77 K [29,37]. The relative pressure (p/p°) range of N_2 was 10^{-7}–1. To prevent elutriation of solid particles from the electrode, we set the evacuation crossover pressure to the fine powder mode. The pore size distribution was calculated by the non-local density functional theory (NLDFT) assuming the slit pore shape for the electrode pores [38]. The total pore volume was determined from the total adsorption at a relative pressure $p/p^{\circ} = 0.99$. The micropore surface area and micropore volume were quantified as the cumulative values corresponding with pores with widths of 2 nm or less. Two different locations from each electrode were analyzed separately, and the average values of the pore volume, surface area, and pore size distribution were reported.

Electrochemical characterization of the electrodes was performed after CDI operation using the potentiostat. The cell was set up as a two-electrode cell with the cathode as the working electrode and the anode as the counter and reference electrodes [39]. The electrolyte was kept the same as the feeding solution used to perform the CDI experiments (Table 1) but without continuous pumping (batch mode). Due to differences in ionic strength, Solution 1 had the highest solution resistance of the three solutions. To remove ionic strength as a variable, we increased the concentration of NaCl in Solution 1 from 10 mM to 15 mM. This change resulted in comparable ionic conductivity values (~ 1500 μS/cm) across all solutions. The electrochemical testing started with OCV for two hours in order to stabilize the system before performing the targeted electrochemical techniques. Cyclic voltammetry (CV) was conducted using a potential window ranging from −0.5 to +0.5 V at a scan rate of 1 mV s^{-1}. The CV started at 0 V vs OCV and was repeated at least two times. To evaluate cell impedance (e.g., charge transfer resistance, diffusion resistance) in response to precipitate, we conducted whole-cell electrochemical impedance spectroscopy (EIS) at the start and end of the CDI tests. EIS was performed using a frequency range of 2 mHz – 100 kHz with an amplitude signal of 30 mV at 0 V bias. The wide frequency range was necessary to probe electrochemical processes occurring at different time scales [40,41]. The specific capacitance (Cs) of the electrode (F g^{-1}) was calculated from the CV data using Eq. 6 [39,42]. and from the EIS data using Eq. 7 [30].

$$Cs = \frac{\Delta I}{2\,\nu m} \tag{6}$$

where I is the current, ν is the scan rate (V s^{-1}), and m is the active mass of the electrode (g).

$$C\ (\mathrm{F\ g^{-1}}) = \left| \frac{1}{\omega Z''} \right| \tag{7}$$

where Z'' is the imaginary part of the impedance spectra (Ω) and ω is the scanning frequency (Hz). CV and EIS measurements were collected from at least two separate CDI tests (new electrodes were used for each test). The average values of electrode capacitance and resistance are reported.

2.3. CDI desalination performance

We measured effluent conductivity and changes in the concentrations of Na^+ and Ca^{2+} (if applicable) during charging and discharging using ion chromatography (IC; ICS-2000, Thermo Fisher, USA). We developed a method for which the minimum reporting limits of Na^+ and Ca^{2+} were 180 and 40 mg/L, respectively. The IC instrument was calibrated using Na^+ and Ca^{2+} solution standards (Environmental Express, USA). To validate the smallest detectable changes among our samples, we ran several quality controls from a secondary source (Inorganic Ventures, USA). The ion removal capacity (IRC), based on IC measurements, was calculated as the ratio of the mass of ions removed to the total mass of all electrodes in their pristine condition (Eq. 8). We calculated IRC by averaging values from cycles 4, 6, and 8. Electrode mass was determined after oven drying at 105°C for 24 h.

$$\mathrm{IRC}\ (mg\,g^{-1}) = \frac{(C_0 - C_f)\ x\ V}{m} \tag{8}$$

Where C_0 and C_f are the initial and final ion concentrations (mg/L), respectively, during the charging phase. V is the volume of solution (L), and m (g) is the total mass of both electrodes.

Charge efficiency (Λ), which is the ratio of total salt removed to the total charge passing through the cell as current, was calculated as:

$$\Lambda = \frac{Q^{*}F^{*} \int (C_0 - C_t)\ dt}{M^{*} \int i(t)\ dt} \tag{9}$$

where F is the Faraday constant (96,485C mol^{-1}), M is the molecular weight of NaCl (58.5 g mol^{-1}), and i(t) is current (A) at time t (sec).

The saturation index (SI) was obtained by Eq. (10) through Visual MINTEQ software to determine the potential formation of possible solids, taking into account the ionic composition of Solution 3 (Table 1). A positive SI value of a product indicates that the solution is supersaturated with respect to that product, and solids may form. The solution is in equilibrium with a product when the SI is set to 0, while it is undersaturated at negative SI values

$$\mathrm{SI} = log\left(\frac{IAP}{Ksp}\right) \tag{10}$$

Where, IAP is the activity product of the lattice ions of the mineral and Ksp is the solubility product constant.

2.4. Statistical analysis

Analysis of variance (ANOVA) was conducted to examine the statistical significance of the differences in the means between groups. A p-value <0.05 was considered statistically significant. ANOVA was followed by multiple comparison tests (post-hoc Bonferroni tests) to

Table 1
Composition of the feedwater solutions tested in this study.

	pH	Conductivity (μS/cm)	Na^+ (mg/L)	Ca^{2+} (mg/L)	Cl^- (mg/L)	HCO_3^- (mg/L)	Description
Solution 1	8.2 ± 0.1	1184	230	–	355	–	Positive control
Solution 2	8.2 ± 0.1	1650	230	100	533	–	Cation selectivity
Solution 3	8.2 ± 0.1	1510	230	100	355	305	Favorable precipitation

determine significance across groups. Unless otherwise stated, all statistical analyses were carried out using a one-way ANOVA.

3. Results and discussion

3.1. Ion removal and recovery during charging and discharging

We first measured effluent conductivity profiles during the charging/discharging cycles of our three test solutions. During the charging phases in all solutions, the effluent conductivity dropped after voltage application and then slowly increased (Fig. 1). The trend of the increase, however, was dependent on solution chemistry. In Solution 1 (NaCl only; positive control), a typical effluent conductivity trend was observed. The effluent conductivity converged back to the influent conductivity at the end of charging, indicating that the electrodes had reached their adsorption capacity [35]. In Solutions 2 and 3, the effluent conductivity did not follow the same trend as Solution 1. It either increased to values greater than the influent (Solution 2), or plateaued around 100 μS/cm lower than the influent (Solution 3). Conductivity profiles similar to what we observed with Solution 2 have been reported previously and have been attributed to Na^+/Ca^{2+}exchange (ion-swapping) [36,43,44]. Na^+ ions are hypothesized to adsorb first and then exchange with Ca^{2+} over time due to stronger interactions between the divalent ion and electrode [45]. The conductivity profile we observed in Solution 3, wherein ion removal continues beyond the maximum adsorption capacity of the electrodes, is not commonly reported, which suggests that electrosorption was not the only method of ion removal.

We quantified the removals (charging phase) and recoveries (discharging phase) of Ca^{2+} and Na^+ to gain insight into possible removal mechanisms in Solution 3. We focused on the cations and not anions because cations are removed at the cathode, and precipitation, if occurring, was expected to happen only at the cathode due to the local basic pH conditions. In Solution 1, 2.89 ± 0.41 mg Na^+/g-C was removed by the end of the charging phase (Fig. 2A) and 2.12 ± 0.26 mg Na^+/g-C was recovered during discharging (~73 % recovery), which agree with values reported in the literature [5,21,30,31]. When Ca^{2+} was added (Solution 2), Na^+ removal decreased significantly (0.22 ± 0.01 vs. 2.89 ± 0.41 mg/g-C, $p < 0.05$) and was nearly completely recovered during discharging (0.24 ± 0.05 mg/g-C). In that solution, Ca^{2+} removal (2.62 ± 0.05 mg/g-C) was almost identical to recovery (2.54 ± 0.03 mg/g-C, $p = 0.68$), indicating that ion removal in Solutions 1 and 2 was primarily through electrosorption (Fig. 2B). The larger removal of Ca^{2+} than Na^+ in Solution 2 was likely due to ion swapping, which is consistent with prior reports [43,44]. Due to a larger concentration of Na^+ relative to Ca^{2+} in the bulk solution (Ca^{2+}: Na^+ molar ratio was 1:4), Na^+ ions were adsorbed first but then desorbed and

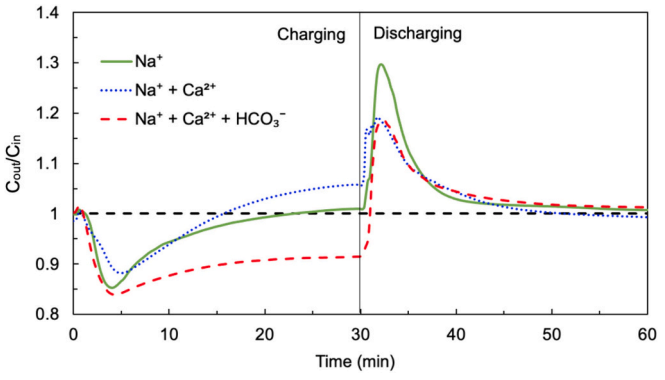

Fig. 1. Effluent solution conductivity profiles (without pH correction) during charging-discharging in the three test solutions; Solution 1 (Na^+), Solution 2 (Na^+ + Ca^{2+}), and Solution 3 (Na^+ + Ca^{2+} + HCO_3^-). Effluent conductivity values were normalized to the influent (initial) conductivity (dotted horizontal black line). Data from cycle 4 of 15 cycles are shown.

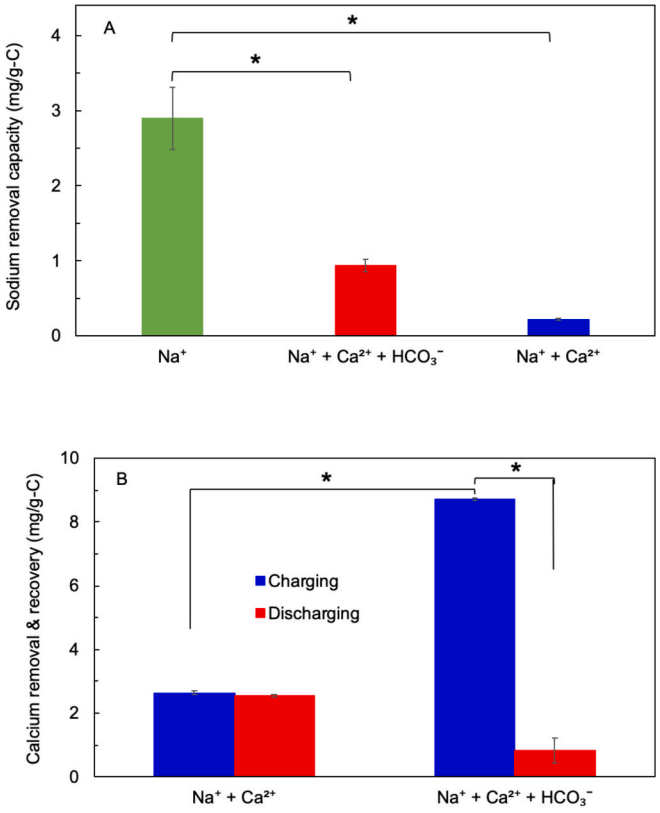

Fig. 2. The total amount of (A) Na^+ and (B) Ca^{2+} (if applicable) removed after CDI tests using Solution 1 (Na^+), Solution 2 (Na^+ + Ca^{2+}), and Solution 3 (Na^+ + Ca^{2+} + HCO_3^-). Error bars show the average of triplicate measurements. The asterisk indicates pairs for which the mean difference was statistically significant. The statistical analysis was carried out using a one-way (part A) and two-way (part B) ANOVA.

replaced by Ca^{2+} ions during the latter part of the charging phase. Seo et al. [26] attributed the replacement "swapping" process to the preferential adsorption for divalent (Ca^{2+}, Mg^{2+}) over monovalent (Na^+) ions when using ACC electrodes. The preferential adsorption was directly linked to ion selectivity, which, in the case of unmodified porous carbon materials, was mainly driven by different physical properties of ions (e.g., valence and electronegativity) [36,46]. Based on this understanding, we expect the preferential adsorption of Ca^{2+} over Na^+ to be a main contributor to the poor Na^+ removal in Solution 2. When both Ca^{2+} and HCO_3^- were added (Solution 3), Na^+ removal decreased significantly compared to Solution 1 (0.94 ± 0.08 vs. 2.89 ± 0.41 mg/g-C, $p < 0.05$). Ca^{2+} removal increased significantly relative to Solution 2 (8.69 ± 0.04 vs. 2.62 ± 0.05 mg/g-C, $p < 0.05$). Only ~ 10 % of Ca^{2+} was recovered during discharging (0.83 ± 0.38 vs. 8.69 ± 0.04 mg/g-C, $p < 0.05$). The poor Ca^{2+} recovery contributed to the smaller curve "area" of the discharging phase in the conductivity profile (Fig. 1) compared to the charging curve. If electrosorption was the primary mechanism of Ca^{2+} removal in Solution 3, a much larger fraction of Ca^{2+} removed should have been recovered. These results indicate that almost all of the Ca^{2+} in Solution 3 was removed by a non-reversible mechanism. To help differentiate reversible (electrosorption) and non-reversible (precipitation) mechanisms in Solution 3, we calculated charge efficiencies. The charge efficiency with Solution 3 exceeded 100 % (152.29 ± 24.41 %) compared to the control (48.51 ± 8.85 %). The latter is consistent with other studies in the literature [21,31]. Importantly, while the charge efficiency during the discharging phase for Solution 1 remained stable at 51.26 ± 16.37 %, it decreased in Solution 3 to 24.71 ± 11.61 %. These results strongly suggest that a non-reversible process occurred in Solution 3 tests.

To help us determine if precipitation on the cathode in Solution 3 was occurring, we conducted a simplified mass balance. Since $CaCO_{3(s)}$ precipitation was the most likely solid to form in that solution based on the SI of possible solids from Visual MINTEQ (**Fig. S1**), we assumed that the unrecovered Ca^{2+} quantity (7.87 ± 0.36 mg/g-C; the difference between the removed and recovered Ca^{2+} during charging and discharging, respectively) was deposited on the electrodes as $CaCO_3$ in each cycle and not released during the discharging phase. Over 15 cycles, the total estimated amount of Ca^{2+} removed was 118.04 ± 5.33 mg/g-C. We compared that value to the dry weight of the cathodes from all solutions before and after CDI operation. No significant differences were observed between the mass of pristine electrodes and cathodes tested with Solutions 1 (0.21 ± 0.00 vs. 0.22 ± 0.01 g, $p = 0.36$) and Solution 2 (0.21 ± 0.00 vs. 0.24 ± 0.02 g, $p = 0.13$) (Fig. 3). In Solution 3, the cathode mass increased significantly by 78.09 ± 19.24 % relative to the pristine electrode (0.37 ± 0.04 vs. 0.21 ± 0.00 g, $p < 0.05$). If we assume the increase in mass was solely due the precipitation of $CaCO_3$ and normalize the mass per gram of total electrode mass, we estimated 134.84 ± 31.76 mg-Ca^{2+}/g-C was deposited. This value is in a good agreement (~12 % difference) with the unrecovered quantity (118.04 ± 5.33 mg/g-C) estimated from the dissolved Ca^{2+} balance using our IC results, especially considering that roughly 10 % Ca^{2+} was recovered during the discharge phases. Overall, these results highlight that the presence of Ca^{2+} reduced Na^+ removals in two different mechanisms: (1) ion exchange in Solution 2, and (2) precipitation of Ca^{2+} onto the cathode in Solution 3.

3.2. Physical changes in the cathode associated with precipitation and their influence on Na^+ removal

Since our results suggested that cathodic $CaCO_3$ precipitation occurred during the charging phase, we conducted additional analyses to determine the mechanisms underpinning the associated reduction in Na^+ adsorption.

3.2.1. Electrode surface properties

We collected SEM images of the electrodes before and after testing each solution to determine if crystalline structures consistent with the morphology of $CaCO_3$ were present on the fibers. The pristine electrodes were devoid of crystals, but had some impurities, including what appeared to be dust and/or organic particles (Fig. 4A) [29,38]. The cathodes from Solutions 1 and 2 were similar to the pristine electrode except for noticeable white layers covering some of the fibers. Based on elemental mapping with EDS, those layers were likely residual NaCl (Fig. 4B&C; the EDS map spectra are shown in **Fig. S2**). The residual NaCl was expected because the cathodes were not rinsed with DI water after disassembling the cell and before drying. The anodes from Solutions 1 and 2 were identical to the cathodes from those solutions, and also appeared to have residual NaCl (**Fig. S3A**). The cathode surface from Solution 3 was dramatically different. EDS revealed that Ca was present on the cathode surface (**Fig. S2C**). The SEM showed that the cathode fibers were partially covered by crystals consisting of two main shapes (cube-like and cauliflower-like) and ranged in size from 10 to 30 μm (Fig. 4D). The crystals appeared attached to the surface, and in many cases wrapped partially or completely around the fibers. Very little stacking of crystals on top of each other was observed, suggesting that contact with the fiber was important for their formation. There are three polymorphs of $CaCO_{3(s)}$: vaterite, calcite, and aragonite, with the last two being the most stable thermodynamic structures [47,48]. The typical shape of calcite and aragonite are "cube-like" and "needle-like", respectively, but the latter structure may change to "cauliflower" under certain crystallization conditions [49]. EDS confirmed that Ca, C, and O were present in the solids, strongly suggesting that the precipitates were $CaCO_3$. We did not observe any solids on the anode from Solution 3 (**Fig. S3B**), which indicates that precipitation of $CaCO_{3(s)}$ was confined to the cathode. We did not observe precipitation in the feed solution although the measured pH at the influent (8.2 ±0.1) was greater than the theoretical pH value (7.3) where $CaCO_3$ precipitation should occur for the chemistry of Solution 3. The pH at the cathode was likely higher and improved the favorability and kinetics of the reaction. We hypothesize that the underlying mechanism driving the pH increase is electrochemical reduction of dissolved oxygen. In our prior study using an identical FT-CDI cell and a NaCl solution, we observed a pH increase upwards of 10, a decrease in DO, production of H_2O_2 and OH^-, and cathode potential of around −0.6 V (vs Ag/AgCl) during charging at 1.2 V [21]. These observations support the occurrence of the reactions in Eqs. (11) & (12).

$$O_2 + 2H^+ + 2e^- \Leftrightarrow H_2O_2 E = 0.69 \text{ V/SHE} \quad (11)$$

$$O_2 + 2H_2O + 4e^- \Leftrightarrow 4OH^- E = 0.40 \text{ V/SHE} \quad (12)$$

When OH^- is generated at the cathode, it can shift the carbonate system speciation from HCO_3^-, which was initially present in the feedwater as $NaHCO_3$, to CO_3^{2-}. Although $NaHCO_3$ can help buffer pH, we hypothesize that at the electrode surface there was a dramatic increase in OH^- due to the local electrochemical reactions in Eqs. (11) & (12). The shift to CO_3^{2-} resulting from the pH increase coupled with a high concentration of Ca^{2+} on/near the cathode due to electrosorption likely promoted the precipitation of $CaCO_{3(s)}$ (Fig. 5). We expect that the buildup of $CaCO_{3(s)}$ occurred gradually over the 15 cycles. Another possible factor that contributed to precipitation over the 15 cycles was the gradual accumulation of Ca^{2+} on/in the cathode. CDI electrodes can electrosorb ions during charging but typically do not fully desorb the ions during discharging [21,31]. We do not expect anodic driven reactions to impact local precipitation at the cathode in our setup because advective flow transported any anode reaction products (e.g., acidity) away from the cathode.

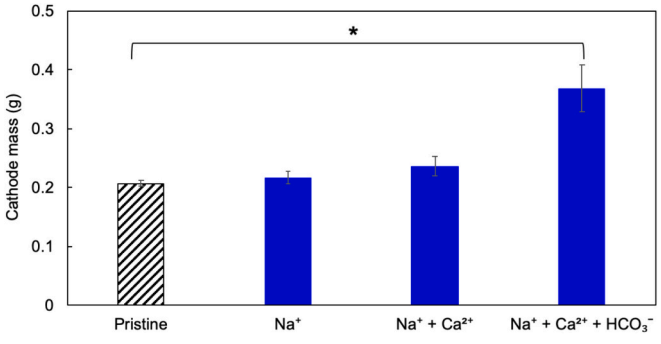

Fig. 3. Cathode mass in its pristine condition and after the 15 CDI cycles with Solution 1 (Na^+), Solution 2 (Na^+ + Ca^{2+}), and Solution 3 (Na^+ + Ca^{2+} + HCO_3^-). Error bars show the average of duplicate measurements. The asterisk indicates the pairs for which the mean difference was statistically significant.

3.2.2. Electrode pore structure

To determine if the $CaCO_{3(s)}$ deposits affected the available pore volume where ions electrosorb, we conducted nitrogen gas sorption analyses. Regardless of the solution composition, we observed a rapid uptake of nitrogen gas at pores with widths <2 nm followed by a plateau at larger pores (type 1 isotherm shape) (Fig. 6). This trend is consistent with micropores dominating the total pore composition [50,51]. The total pore volume of the pristine electrode was 0.64 ± 0.01 cm^3/g, which agrees with values reported in the literature [29,38]. No significant difference was observed in the total pore volume of the cathode from Solution 1 and the pristine electrode (0.64 ± 0.06 vs. 0.64 ± 0.01 cm^3/g, $p = 0.83$). The total pore volume of the cathode from Solution 2 was smaller, but not significantly different than the pristine electrode (0.57 ± 0.00 vs. 0.64 ± 0.01 cm^3/g, $p = 0.06$). One possible explanation for the decrease in pore volume of the cathode tested with Solution 2 is precipitation of one or more Ca^{2+}-based solids. Although we did not add

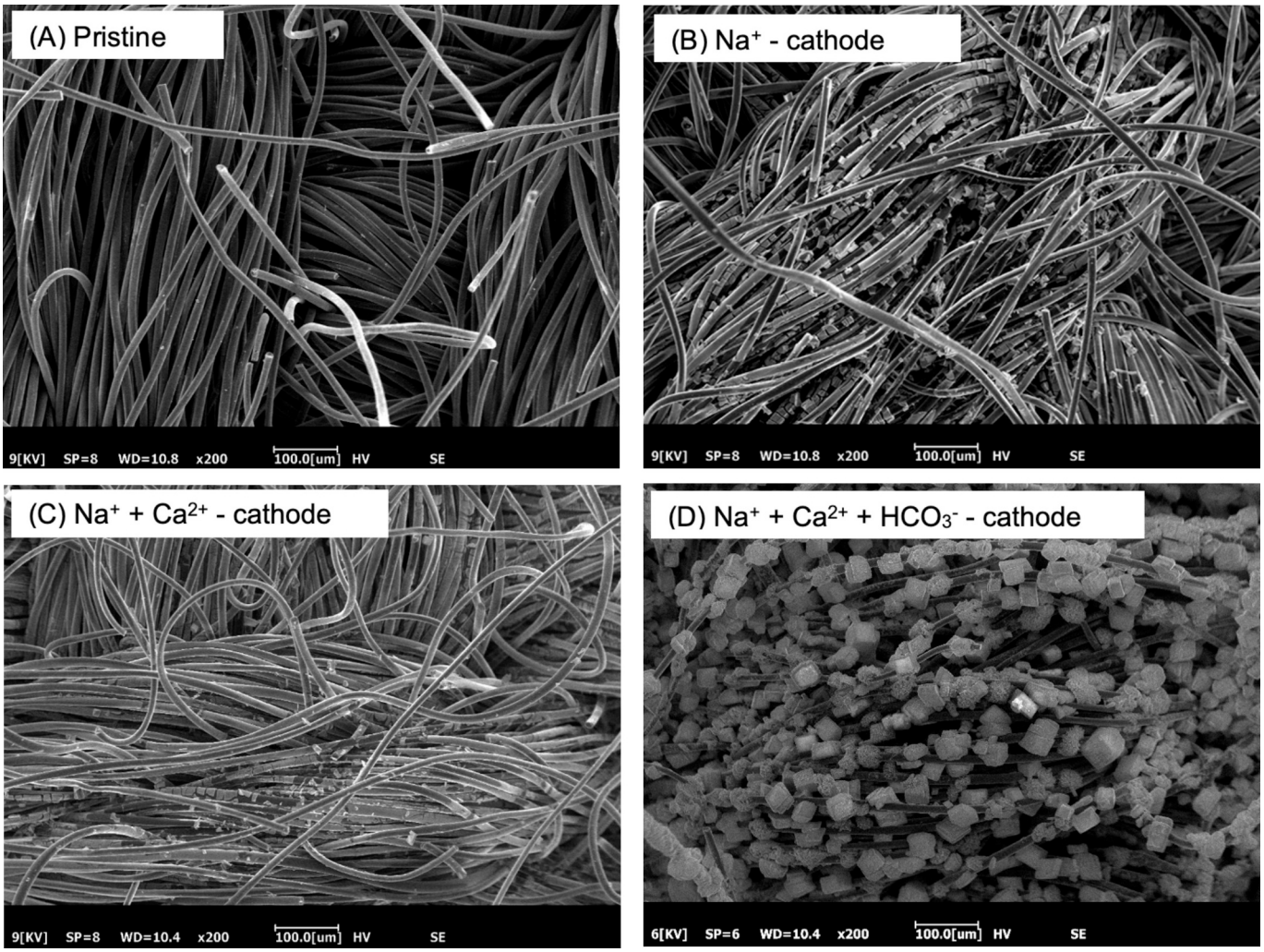

Fig. 4. SEM images of (A) a pristine AC electrode and the cathodes after finishing CDI tests with (B) Solution 1 (Na^+), (C) Solution 2 ($Na^+ + Ca^{2+}$), and (D) Solution 3 ($Na^+ + Ca^{2+} + HCO_3^-$).

HCO_3^-, it is possible that CO_2 from the atmosphere dissolved into the feedwater and provided a source of carbonate (CO_2 in water results in carbonic acid, which can then dissociate into H^+, HCO_3^-, and CO_3^{2-} depending on pH) [52]. Assuming the concentration of CO_2 in the air during the tests was 400 ppm and a Henry's Law constant of 29.41 atm/M for CO_2 at $T = 25$ °C, we estimate that 0.01 mM of dissolved CO_2 may have been present. That dissolved CO_2 might have contributed to low levels of $CaCO_3$ precipitation. It is also possible that $Ca(OH)_{2(s)}$ formed due to local electrogeneration of OH^- from the reduction of dissolved oxygen although we found, based on thermodynamic predictions, that solid was not favorable under our experimental conditions in Solution 3 (**Fig. S1**) [53]. The pore volume of the cathode from Solution 3 was much different from all the others. It was significantly smaller than the pristine control (0.41 ± 0.03 vs. 0.64 ± 0.01 cm^3/g, $p < 0.05$) and the cathodes from Solution 1 (0.41 ± 0.03 vs. 0.64 ± 0.05 cm^3/g, $p < 0.05$) and Solution 2 (0.41 ± 0.03 vs. 0.57 ± 0.00 cm^3/g, $p < 0.05$).

We also observed significant decreases in the micropore volume and specific surface area of the cathode from Solution 3. The micropore volume decreased significantly from 0.53 ± 0.00 cm^3/g in the pristine electrode to 0.37 ± 0.00 cm^3/g with Solution 3 ($p < 0.05$). That decrease contributed to 72.7 % of the reduction in total pore volume. Compared to the pristine electrode, the cathode from Solution 3 had a 34.4 ± 1.29 % smaller specific surface area (1002.21 ± 30.1 vs. 1527.6 ± 15.76 m^2/g, $p < 0.05$). We attribute the reduction in the micropores to non-porous $CaCO_{3(s)}$ crystals covering the carbon fiber surface and in turn blocking the pores [54]. Pore blocking would (1) reduce the number of open sites available in the cathode for electrosorption and (2) limit the accessibility of ions toward electroactive sites in the micropores [55]. These hypotheses are consistent with the decreased Na^+ adsorption in Solution 3, relative to Solution 1, and supported by other studies where severe declines in desalination performance were linked to electrode fouling and deterioration in the pore structure [28,37,56].

The physical properties of the anode from Solution 3 did not change significantly compared to the pristine, confirming that the impact of precipitation on the pore structure was unique to the cathode. Unlike the cathode, the anode from Solution 3 had a pore structure that was consistent with the pristine control (**Fig. S4**). The total pore volume decreased slightly from 0.64 ± 0.01 cm^3/g (pristine) to 0.62 cm^3/g while the micropore volume remain unchanged at 0.53 cm^3/g. These results suggested that micropores (pores with < 2 nm in diameter) did not contribute to the slight reduction in the total pore volume, and that mesopores (2 nm < pore size <50 nm) actually caused that change. This small change in mesopores, but not the micropores, is possibly due to carbon oxidation at the anode, which can damage the surface of the anode [57,58]. Carbon-based electrodes can undergo oxidation through electrochemical and chemical means [59–62]. Electrochemical oxidation typically affects micropores more than mesopores because micropores have high surface area-to-volume ratio and are more reactive to surface modifications caused by electrochemical oxidation. Mesopores are generally more susceptible to aqueous-phase chemical oxidation

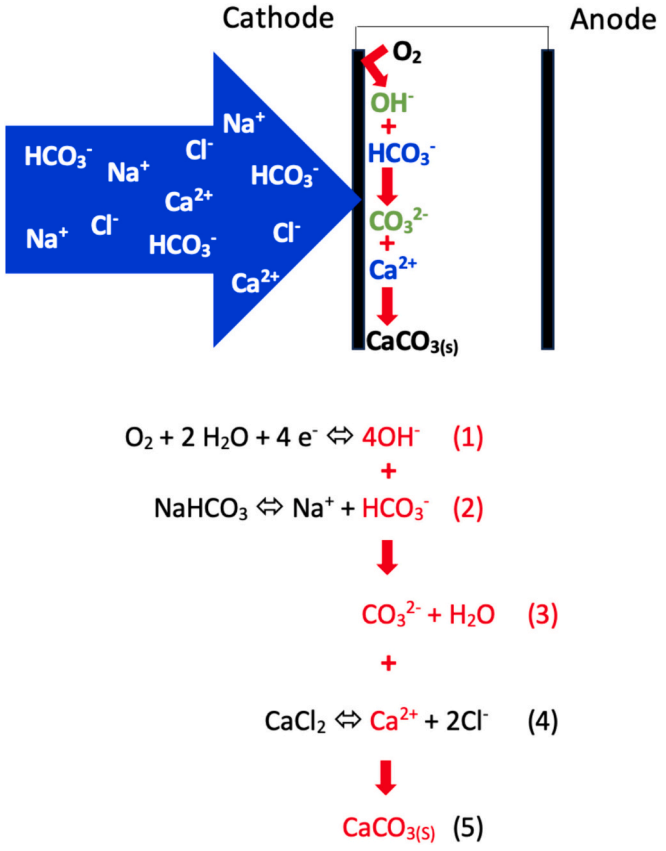

Fig. 5. Conceptual diagram showing the hypothesized pathway of calcium carbonate precipitation in the flow-through CDI (FT-CDI) cell. In (1), OH^- is produced during dissolved oxygen reduction. The HCO_3^- (2) shifts to CO_3^{2-} (3) due to the increase in pH. Ca^{2+} (4) reacts with CO_3^{2-} to form $CaCO_3$ (5).

because they provide higher accessibility to electrolytes (i.e., the larger mesopores make it easier for chemicals to reach exposed surfaces than micropores). Hydrogen peroxide is typically generated at the upstream cathode in FT-CDI and transported toward the downstream anode [21]. Since our cell positioned the anode downstream, we hypothesize H_2O_2-driven oxidation of the anode was the primary mechanism of oxidation. Our results overall show that in the solution chemistry that was most favorable for formation of $CaCO_{3(s)}$, there were significant decreases in micropore volume and surface area at the cathode.

3.3. Electrochemical properties

3.3.1. Cell capacitance

If precipitate formation was blocking pores on the cathode, we hypothesized that cell capacitance should decrease. To address this hypothesis, we performed in situ CV (whole-cell) immediately after the 15 cycles finished. CV can show the capacity of the electrode to accumulate ions in the electrical double layer at the electrode/electrolyte interface [12]. All of our CV curves showed a typical capacitive behavior without oxidation or reduction peaks (Fig. 7). The internal area of the curves changed with solution chemistry. The specific capacitance derived from the CV curves using Eq. 6 was 65.84 ± 0.26 F g^{-1} prior to the CDI cycling and slightly decreased to 63.84 ± 3.12 F g^{-1} after testing Solution 1 and 62.75 ± 8.19 F g^{-1} with Solution 2, which, based on statistical analysis, were not significantly different ($p = 0.87$). The cell capacitance in Solution 3, however, was significantly smaller than any other case, i.e., Solution 1 (29.95 ± 5.97 vs. 63.84 ± 3.12 F g^{-1}, $p < 0.05$). We attribute the lower capacitance in Solution 3 primarily to the deposition of non-conductive and non-porous $CaCO_{3(s)}$ on the electrode surface. This result is consistent with a prior report of capacitance decrease of AC electrodes when Fe-based precipitates formed on the electrode surface [63]. We did not observe a complete loss of capacitance, likely due to the partial surface coverage of the electrode with precipitates. Our SEM images confirmed that some surface area and pores remained available. Nevertheless, we show that after only 15 h of operation, significant capacitance losses can occur in solution chemistries that favor precipitation.

3.3.2. Cell resistance

EIS probes electrochemical processes occurring on different time scales using a wide range of frequency scanning. The frequencies at which EIS is obtained are typically divided into three regions (high, intermediate, and low) in the Nyquist plot [64–67]. The Nyquist plots of our cells displayed the same key features before and after CDI operation in each solution: a semicircle in the high frequency range, followed by a line with two different slopes in the intermediate and low frequency domains (Fig. 8). We fitted our plots with an equivalent circuit model consisting of a series resistance (*Rs*), constant phase element (*Q*), charge transfer resistance (R_{ct}), and Warburg element (Z_w) (**Fig. S5**) [40,68,69]. Since the electrolyte solution under which EIS measurements were collected was not a perfect conductor of charge [some energy was lost due to solution resistance caused by the low ionic strength of the tested solutions (~ 15 mM NaCl)], a resistor was added in series, *Rs*, to estimate bulk solution resistance between the electrodes. At the interface of a charged electrode, two phases with opposite charges (e.g., anode and anions) separated by water molecules (dielectric) formed a capacitor. We used *Q* to model the capacitance of the capacitor (electrodes) to store charges because the CDI electrodes were non-ideal capacitors (the carbon material creates resistance while passing charges). The non-ideal capacitor was connected in parallel with R_{ct} to characterize impedance due to polarization (charge transfer). To account for electrochemical processes occurring at the electrode surface that were limited by diffusion (the line with a slope changing from 45° toward 90° after the semicircle), Z_w was included in the equivalent circuit.

After fitting our model, we then calculated each component of total resistance before and after the CDI tests. Prior to the tests (at OCV), we did not observe noticeable differences in impedance across all solutions, which was expected because the ionic strength, electrodes, and cell setup used were the same. All impedance values were averaged ($n = 3$) and reported as the initial value (Fig. 9). After the CDI tests, R_s remained stable and nearly identical among the solutions (4.72 ± 0.2 to 4.44 ± 0.18, 4.88 ± 0.08, and 4.62 ± 0.04 Ω after testing with Solutions 1, 2 and 3, respectively) (Fig. 9A), which was expected because of the similar ionic strength across solutions. Other components of impedance did change significantly. For example, R_{ct} increased after operation in all solutions, but the magnitude was largest after testing with Solution 3 (Fig. 9B). Prior to the tests, R_{ct} was 1.89 ± 0.22 Ω. After the tests in Solution 1, it increased to 2.39 ± 0.29 Ω ($p = 0.24$), and after Solution 2, it increased to 2.36 ± 0.17 Ω ($p = 0.25$). The increase in R_{ct} values after testing with Solutions 1 and 2 were likely due to carbon oxidation at the anode. EIS was performed on the whole cell, so changes in impedance could be caused by changes at the cathode and/or anode [32,70]. Tests with Solution 3 were associated with a significant increase in R_{ct} (3.54 ± 0.25 vs. 1.89 ± 0.22 Ω, $p < 0.05$) (Fig. 9B). Assuming that the increase in R_{ct} due to changes in the anode were similar across the solutions, we hypothesize that the major contributor to the increase was precipitation of $CaCO_3$ on the cathode. $CaCO_3$ is not electrically conductive. The attachment of non-conductive crystals to the carbon fibers likely increased the intrinsic resistivity of the electrode to transfer charge. Marín-Cruz et al. [71,72] showed that deposition of $CaCO_{3(s)}$ crystals on carbon steel electrodes produced a resistive layer on the electrode surface and increased the charge transfer resistance. It is also possible that the precipitated solids may have decreased the electrode/current collector contact area, increasing the contact resistance [73].

We also observed a similar trend with the diffusion resistance R_{diff}. R_{diff} was 3.86 ± 0.22 Ω prior to the tests. It decreased, but not

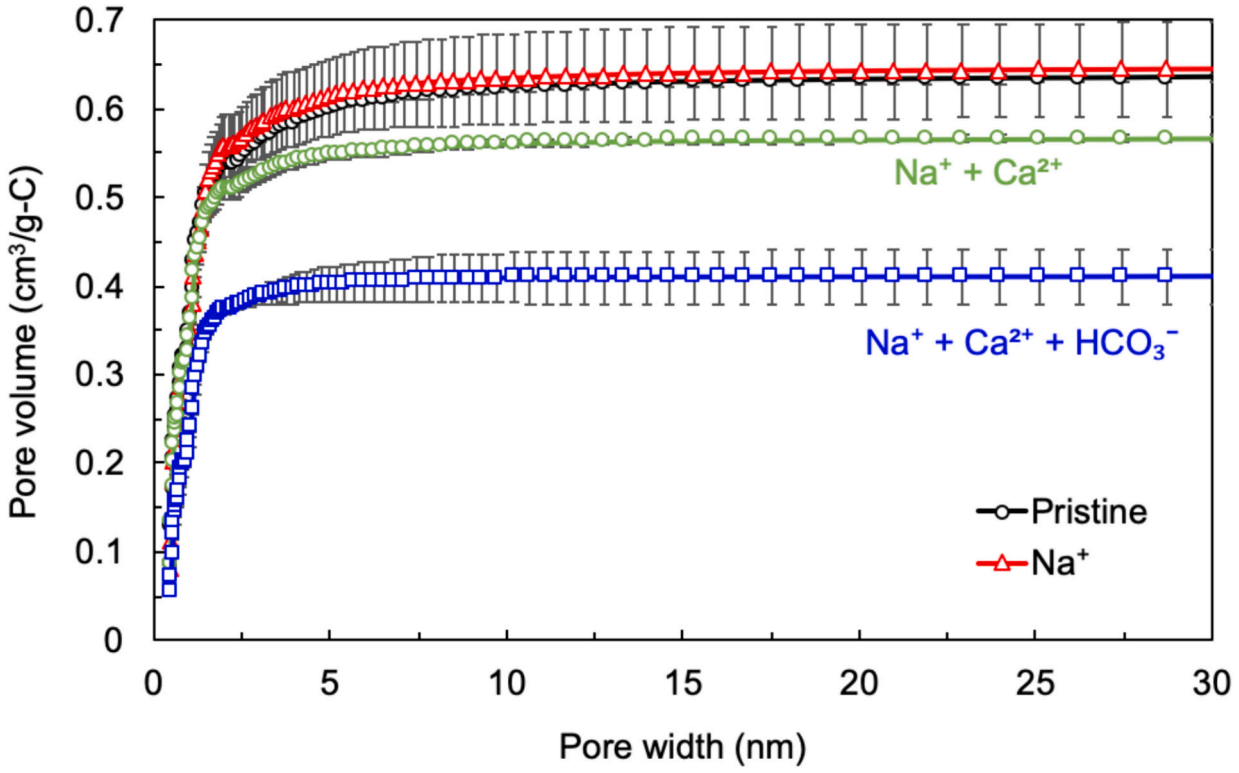

Fig. 6. Measured cumulative pore volume versus pore width of the pristine and cycled cathodes with Solution 1 (Na^+), Solution 2 ($Na^+ + Ca^{2+}$), and Solution 3 ($Na^+ + Ca^{2+} + HCO_3^-$). Error bars show the average of duplicate measurements.

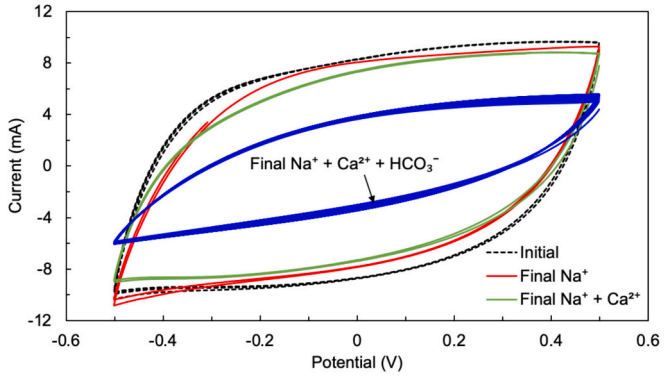

Fig. 7. Cyclic voltammetry of the CDI cells at the start of the test (black dashed line) and after completing the 15 cycle tests. The red solid line represents Solution 1 (Na^+), the green solid line shows Solution 2 ($Na^+ + Ca^{2+}$), and the blue solid line shows Solution 3 ($Na^+ + Ca^{2+} + HCO_3^-$).

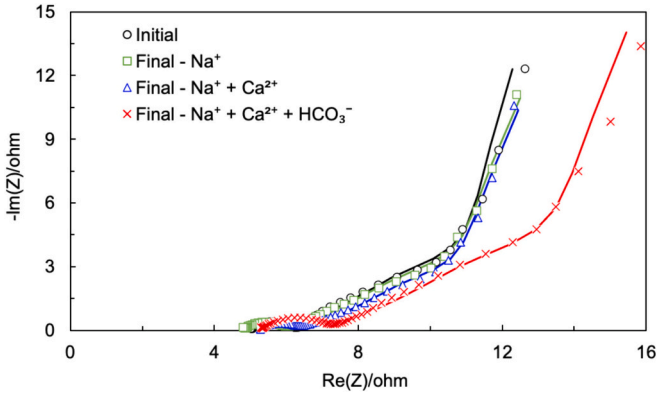

Fig. 8. Nyquist plots of the CDI cells at the start of the tests (black circles) and after the 15 cycle tests for Solution 1 (green squares; Na^+), Solution 2 (blue triangles; $Na^+ + Ca^{2+}$), and Solution 3 (red Xs; $Na^+ + Ca^{2+} + HCO_3^-$).

significantly, to 3.65 ± 0.21 Ω after testing with Solution 1 ($p = 0.34$) and to 3.4 ± 0.24 after cycling with Solution 2 ($p = 0.07$). In Solution 3, however, R_{diff} increased significantly to 4.78 ± 0.21 Ω ($p < 0.05$) (Fig. 9C). Intermediate-frequency based diffusion resistances are caused by many factors including the electrolyte, electrode properties, system setup, and temperature [66,67]. Lenz et al. [65] showed that in porous electrodes the pore size distribution played an important role in transport by diffusion not just within the electrode pores, but also from the bulk electrolyte toward the electrode interface. They concluded that AC electrodes mainly composed of micropores, despite having a large pore volume, surface area, and specific capacitance, had greater R_{diff} values than carbon aerogels with much wider pores. The authors attributed this to the dense fibers oriented in macroscopic strands in the AC electrodes, which hindered ion accessibility into the micropores of the inner fibers.

The large amount of larger mesopores in the carbon aerogel electrode reportedly allowed easier access of ions toward and within the carbon aerogel. Nian et al. [66] suggested that the presence of nonuniform pathways for ion transport from the bulk electrolyte into the porous electrode caused by nonuniform electrode pore size and electrode roughness may contribute to increases in R_{diff}. Based on these prior observations, we attribute the large R_{diff} value measured in Solution 3 to (1) pore blockage by the crystals, (2) large reductions in the "active" area available for ion transport from the bulk toward the electrode interface, and (3) longer and nonuniform pathways for diffusion of ions to the inner pores (micropores) in the carbon fibers.

The impedance in the low frequency range, which is indicative of the double layer capacitance of carbon electrodes, of Solution 3 was also appreciably different from the other solutions. A non-vertical line was observed in all solutions, but the deviation from ideal capacitor behavior

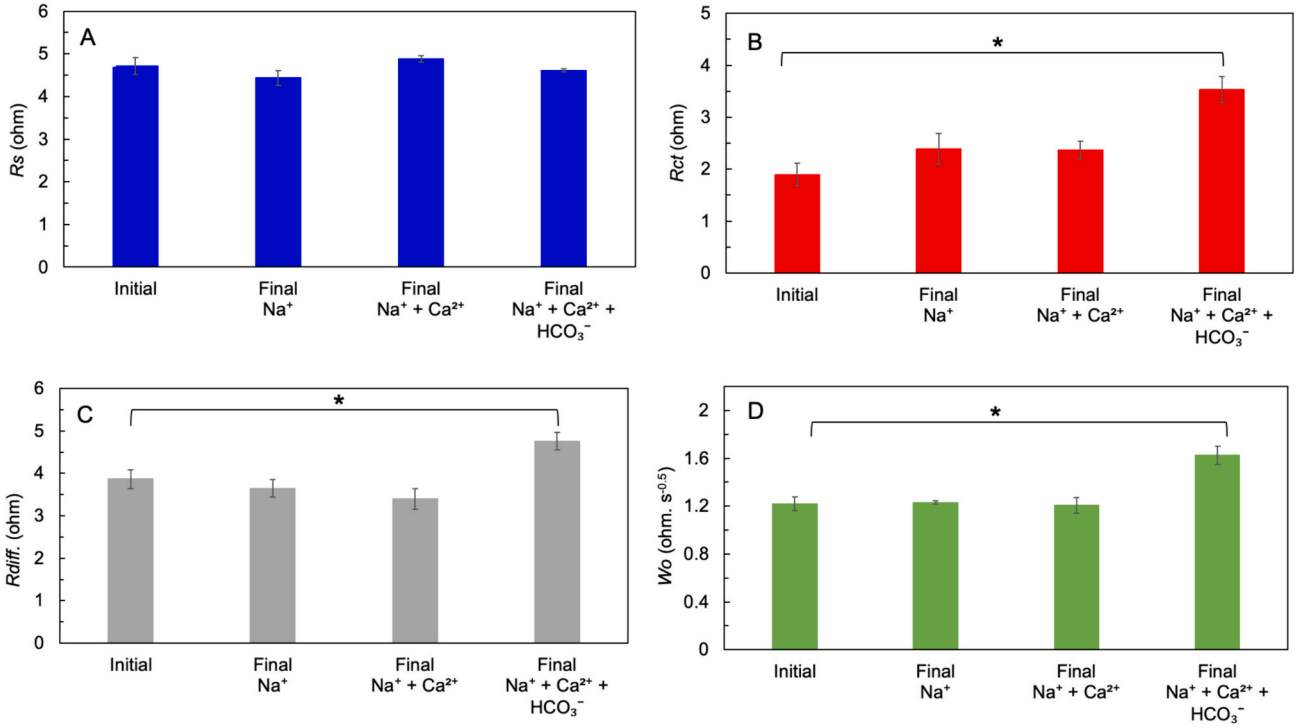

Fig. 9. Summary of the EIS fitting results of (A) solution resistance, R_s (B) charge transfer resistance, R_{ct} (C) diffusion resistance, R_{diff} and (D) Warburg coefficient, W_o, for the CDI cell in initial and final test conditions using Solution 1 (Na^+), Solution 2 ($Na^+ + Ca^{2+}$), and Solution 3 ($Na^+ + Ca^{2+} + HCO_3^-$). Since EIS was performed on the whole CDI cell, changes in impedance values after CDI cycling were due to changes in the cathode and/or anode electrodes. Error bars show the average of duplicate measurements. The asterisk indicates the pairs for which the mean difference is statistically significant.

was much more pronounced after testing with Solution 3. Deviations from a vertical line is indicative of decreased capacitance. We found from the Nyquist fitting that the Q value (representing the capacitance) for the pristine control ($0.06 \pm 0.00\ \Omega^{-1}$ s) decreased slightly, but not significantly, to $0.06 \pm 0.01\ \Omega^{-1}$ s ($p = 0.22$) and $0.05 \pm 0.01\ \Omega^{-1}$ s ($p = 0.08$) after testing Solutions 1 and 2, respectively. Solution 3, however, resulted in a 38.3 ± 0.05 % decrease in capacitance relative to the pristine condition ($0.04 \pm 0.00\ \Omega^{-1}$ s), which, based on statistical analysis, was significantly different ($p < 0.05$). We also measured the cell capacitance from EIS using Eq. 7 and observed a similar trend in the low frequency range (**Fig. S6**). In particular, the capacitance at the minimum frequency (2 mHz) was 52.02 ± 1.91 F/g-C in the initial stage, 54.88 ± 0.89 F/g-C after testing with Solution 1, 55.49 ± 3.51 F/g-C in post-experiment of Solution 2, and 44.83 ± 1.77 F/g-C after testing with Solution 3. These results were also consistent with the specific capacitance values obtained from the CV measurements.

The deviation from the vertical line in the low frequency range is also a sign of increased diffusive resistivity into and inside the pore structures. The extent of deviation (the slope of the line in the low frequency region, beyond the "knee" frequency) is equal to the Warburg coefficient (W_o). The initial W_o value was $1.22 \pm 0.06\ \Omega\ s^{-0.5}$. Larger W_o values imply slower ion diffusion rates within the electrode pores [66–69]. While cells tested with Solutions 1 and 2 had W_o values that were more stable with no statistically significant differences relative to the initial values [1.23 ± 0.01 (Solution 1) vs. $1.22 \pm 0.06\ \Omega\ s^{-0.5}$, $p = 0.83$ and 1.21 ± 0.07 (Solution 2) vs. $1.22 \pm 0.06\ \Omega\ s^{-0.5}$, $p = 0.8$], cells cycled with Solution 3 were not (Fig. 9D). W_o increased by 33.2 ± 6.4 % relative to the initial condition to $1.63 \pm 0.08\ \Omega\ s^{-0.5}$, which, based on statistical analysis, was significantly different ($p < 0.05$) (Fig. 9D). These findings suggest that the deposition of non-porous $CaCO_3$ crystals on the carbon fibers decreased the mobility of ions toward the electrode surface and/or within the inner pores. Further support of this is the low diffusion coefficient and large W_o reported in porous carbon electrodes suffering from nonuniform pathways of ions and electrode pore size [64].

The AC material used in this study is not an ideal capacitor under our experimental conditions, even in the pristine condition (as expressed by the non-vertical line in the low frequency region) due to inherent diffusion resistance of ions through the inner pores caused by the highly dense fibers [65]. We expect the deposition of non-porous $CaCO_{3(s)}$ on the carbon fibers to further restrict ion movement (increased resistance) and result in insufficient pore utilization (decreased capacitance). Our impedance results highlight that the deposition of non-conductive, non-porous particles on the electrode surface increased the impedance of several electrochemical processes (R_{ct}, R_{diff}, Z_w, and Q). Higher resistance in turn contributed to lower Na^+ adsorption capacity.

4. Conclusions

Our overall objective was to determine the potential for in situ precipitation on electrodes in flow-through capacitive deionization (FT-CDI) and its impact on desalination. We used a solution chemistry that mimicked two key components in real brackish waters that can result in precipitation of the model solid $CaCO_3$: Ca^{2+} and HCO_3^-. We quantified the impact of precipitation on desalination performance based on Na^+ adsorption and evaluated the stability of the electrode and FT-CDI cell through several physical and electrochemical measurements. Our major findings are summarized as follows;

- In the absence of precipitation (only NaCl present), 2.89 ± 0.41 mg Na^+/g-C was removed. Under solution conditions that could form $CaCO_{3(s)}$ when elevated pH occurred, Na^+ adsorption was reduced by up to ~67 % (0.94 ± 0.08 mg/g-C).
- Scanning electron microscopy images showed that the cathode tested in a solution containing Ca^{2+} and HCO_3^- was partially covered by morphologies consistent with calcite and aragonite crystals. These crystals were not observed on the cathodes in the absence of HCO_3^- nor on any of the anodes across all solutions tested.

- Precipitation on the cathode fibers was associated with a ~ 73 % decrease in micropore volume. The decrease in accessibility of these pores by ions likely contributed to the decline in Na^+ removal.
- Lower electrode capacitance and larger resistance were associated with $CaCO_{3(s)}$ precipitation. The deposition of non-conductive and non-porous $CaCO_{3(s)}$ crystals likely decreased electrode conductivity and capability for charge transfer and ion transport.
- The physical and electrochemical properties of the anode remained stable after cycling, indicating that the reduced desalination performance was primarily due to the cathode and precipitate formation.
- Strategies to reduce or reverse precipitation and regenerate the electrosorption capacity of electrodes are needed to minimize the detrimental impact of precipitation on electrode stability and salt removal. Examples of strategies include alternating the polarity of electrodes while cycling and reducing the charging cycle time and/or charging voltages.

CRediT authorship contribution statement

Yazeed Algurainy: Visualization, Validation, Resources, Methodology, Investigation, Formal analysis, Data curation, Conceptualization, Writing – review & editing, Writing – original draft. **Douglas F. Call:** Supervision, Resources, Project administration, Funding acquisition, Formal analysis, Conceptualization, Writing – review & editing, Writing – original draft.

Declaration of competing interest

The authors declare that they have no known competing financial interests or personal relationships that could have appeared to influence the work reported in this paper.

Data availability

Data will be made available on request.

Acknowledgements

This research was supported by King Saud University (KSU), Saudi Arabia. The authors would like to thank Deanship of scientific research in KSU for funding and supporting this research through the initiative of DSR Graduate Students Research Support (GSR). The authors thank Dr. Lisa Castellano for help in running the ion chromatography measurements. The authors also thank Mr. Charles Mooney and Mr. Roberto Garcia from the Analytical Instrumentation Facility (AIF) at North Carolina State University for help in analyzing the morphology of the electrodes in this study. The AIF is supported by the State of North Carolina and the National Science Foundation (award number ECCS-2025064). The AIF is a member of the North Carolina Research Triangle Nanotechnology Network (RTNN), a site in the National Nanotechnology Coordinated Infrastructure (NNCI). This work was intellectually advanced through, and benefited from, collaborations with the Science and Technologies for Phosphorus Sustainability (STEPS) Center (NSF award number CBET-2019435).

Appendix A. Supplementary data

Supplementary data to this article can be found online at https://doi.org/10.1016/j.desal.2024.117853.

References

[1] Y. Lei, E. Geraets, M. Saakes, R.D. van der Weijden, C.J.N. Buisman, Electrochemical removal of phosphate in the presence of calcium at low current density: precipitation or adsorption? Water Res. 169 (2020) 115207.
[2] P. Liu, et al., Graphene-based materials for capacitive deionization, J. Mater. Chem. A 5 (2017) 13907–13943.
[3] Z.H. Huang, Z. Yang, F. Kang, M. Inagaki, Carbon electrodes for capacitive deionization, J. Mater. Chem. A 5 (2017) 470–496.
[4] Q. Wu, et al., Enhanced capacitive deionization of an integrated membrane electrode by thin layer spray-coating of ion exchange polymers on activated carbon electrode, Desalination 491 (2020) 114460.
[5] E.M. Remillard, A.N. Shocron, J. Rahill, M.E. Suss, C.D. Vecitis, A direct comparison of flow-by and flow-through capacitive deionization, Desalination 444 (2018) 169–177.
[6] Y. Zhang, et al., Fabrication of porous graphene electrodes via CO2 activation for the enhancement of capacitive deionization, J. Colloid Interface Sci. 536 (2019) 252–260.
[7] M. Shi, et al., Construction and evaluation of a novel three-electrode capacitive deionization system with high desalination performance, Sep. Purif. Technol. 273 (2021) 118976.
[8] E. Liu, L.Y. Lee, S.L. Ong, H.Y. Ng, Treatment of industrial brine using capacitive deionization (CDI) towards zero liquid discharge – challenges and optimization, Water Res. 183 (2020) 116059.
[9] P.M. Biesheuvel, S. Porada, J.E. Dykstra, The difference between Faradaic and non-Faradaic electrode processes. 1–16 (2018).
[10] W. Xing, et al., Versatile applications of capacitive deionization (CDI)-based technologies, Desalination 482 (2020).
[11] J. Choi, P. Dorji, H.K. Shon, S. Hong, Applications of capacitive deionization: desalination, softening, selective removal, and energy efficiency, Desalination 449 (2019) 118–130.
[12] M.C. Zafra, P. Lavela, C. Macías, G. Rasines, J.L. Tirado, Electrosorption of environmental concerning anions on a highly porous carbon aerogel, J. Electroanal. Chem. 708 (2013) 80–86.
[13] A. Hassanvand, G.Q. Chen, P.A. Webley, S.E. Kentish, A comparison of multi-component electrosorption in capacitive deionization and membrane capacitive deionization, Water Res. 131 (2018) 100–109.
[14] Z. Chen, H. Zhang, C. Wu, Y. Wang, W. Li, A study of electrosorption selectivity of anions by activated carbon electrodes in capacitive deionization, Desalination 369 (2015) 46–50.
[15] P. Xu, J.E. Drewes, D. Heil, G. Wang, Treatment of brackish produced water using carbon aerogel-based capacitive deionization technology, Water Res. 42 (2008) 2605–2617.
[16] Seed, L. P., Yetman, D. D., Pargaru, Y. & Shelp, G. S. The Desel System–Capacitive Deionization for the Removal of Ions From Water. Proc. Water Environ. Fed. 2006, 7172–7180 (2014).
[17] T.J. Welgemoed, C.F. Schutte, Capacitive deionization technologyTM: an alternative desalination solution, Desalination 183 (2005) 327–340.
[18] Lei, Y., Song, B., Weijden, R. D. Van Der, Saakes, M. & Buisman, C. J. N. Electrochemical Induced Calcium Phosphate Precipitation: Importance of Local pH. (2017). doi:https://doi.org/10.1021/acs.est.7b03909.
[19] Lei, Y., Zhan, Z., Saakes, M., Weijden, R. D. Van Der & Buisman, C. J. N. Electrochemical recovery of phosphorus from wastewater using tubular stainless-steel cathode for a scalable long-term operation. Water Res. 199, 117199 (2021).
[20] C.J.N. Buisman, Is there a Precipitation Sequence in Municipal Wastewater Induced by Electrolysis?, 2018, https://doi.org/10.1021/acs.est.8b02869.
[21] Y. Algurainy, D.F. Call, Asymmetrical removal of sodium and chloride in flow-through capacitive deionization, Water Res. 183 (2020) 116044.
[22] B. Shapira, E. Avraham, D. Aurbach, Side reactions in capacitive deionization (CDI) processes: the role of oxygen reduction, Electrochim. Acta 220 (2016) 285–295.
[23] N. Holubowitch, A. Omosebi, X. Gao, J. Landon, K. Liu, Quasi-steady-state polarization reveals the interplay of capacitive and faradaic processes in capacitive deionization, ChemElectroChem 4 (2017) 2404–2413.
[24] M.M. Benjamin, Water Chemistry, Waveland Press, 2014.
[25] W. Zhang, M. Mossad, L. Zou, A study of the long-term operation of capacitive deionisation in inland brackish water desalination, DES 320 (2013) 80–85.
[26] S. Seo, et al., Investigation on removal of hardness ions by capacitive deionization (CDI) for water softening applications, Water Res. 44 (2010) 2267–2275.
[27] R. Broséus, J. Cigana, B. Barbeau, C. Daines-martinez, H. Suty, Removal of total dissolved solids, nitrates and ammonium ions from drinking water using charge-barrier capacitive deionisation, DES 249 (2009) 217–223.
[28] M. Mossad, L. Zou, Study of fouling and scaling in capacitive deionisation by using dissolved organic and inorganic salts, J. Hazard. Mater. 244–245 (2013) 387–393.
[29] C. Kim, et al., Influence of pore structure and cell voltage of activated carbon cloth as a versatile electrode material for capacitive deionization, Carbon N. Y. 122 (2017) 329–335.
[30] Y. Algurainy, D.F. Call, Improving long-term anode stability in capacitive deionization using asymmetric electrode mass ratios, ACS ES T Eng. 2 (2022) 129–139.
[31] C. Zhang, D. He, J. Ma, W. Tang, T.D. Waite, Comparison of faradaic reactions in flow-through and flow-by capacitive deionization (CDI) systems, Electrochim. Acta 299 (2019) 727–735.
[32] C. Zhang, D. He, J. Ma, W. Tang, T.D. Waite, Faradaic reactions in capacitive deionization (CDI) - problems and possibilities: a review, Water Res. 128 (2018) 314–330.
[33] X. Gao, et al., Capacitive deionization using symmetric carbon electrode pairs, Environ. Sci. Water Res. Technol. 5 (2019) 660–671.
[34] Z.H. Huang, M. Wang, L. Wang, F. Kang, Relation between the charge efficiency of activated carbon fiber and its desalination performance, Langmuir 28 (2012) 5079–5084.

[35] S. Porada, R. Zhao, A. Van Der Wal, V. Presser, P.M. Biesheuvel, Progress in materials science review on the science and technology of water desalination by capacitive deionization, Prog. Mater. Sci. 58 (2013) 1388–1442.
[36] X. Zhang, K. Zuo, X. Zhang, C. Zhang, P. Liang, Selective ion separation by capacitive deionization (CDI) based technologies: a state-of-the-art review, Environ. Sci.: Water Res. Technol. 6 (2020) 243–257.
[37] T. Wang, et al., Scaling behavior of iron in capacitive deionization (CDI) system, Water Res. 171 (2020) 115370.
[38] R. Uwayid, N.M. Seraphim, E.N. Guyes, D. Eisenberg, M.E. Suss, Characterizing and mitigating the degradation of oxidized cathodes during capacitive deionization cycling, Carbon N. Y. 173 (2021) 1105–1114.
[39] Y. Qu, T.F. Baumann, J.G. Santiago, M. Stadermann, Characterization of Resistances of a capacitive deionization system, Environ. Sci. Technol. 49 (2015) 9699–9706.
[40] A.J. Roberts, R.C.T. Slade, Effect of specific surface area on capacitance in asymmetric carbon/α-MnO2 supercapacitors, Electrochim. Acta 55 (2010) 7460–7469.
[41] F. Gao, X. Li, W. Shi, Z. Wang, Highly selective recovery of phosphorus from wastewater via capacitive deionization enabled by ferrocene-polyaniline-functionalized carbon nanotube electrodes, ACS Appl. Mater. Interfaces 14 (2022) 31962–31972.
[42] J.S. Kim, J.H. Choi, Fabrication and characterization of a carbon electrode coated with cation-exchange polymer for the membrane capacitive deionization applications, J. Membr. Sci. 355 (2010) 85–90.
[43] R. Zhao, et al., Time-dependent ion selectivity in capacitive charging of porous electrodes, J. Colloid Interface Sci. 384 (2012) 38–44.
[44] Avraham, E., Yaniv, B., Soffer, A. & Aurbach, D. Developing Ion Electroadsorption Stereoselectivity, by Pore Size Adjustment with Chemical Vapor Deposition onto Active Carbon Fiber Electrodes. Case of Ca 2 +/Na + Separation in Water Capacitive Desali- nation. 7385–7389 (2008).
[45] X. Zhang, K. Zuo, X. Zhang, C. Zhang, P. Liang, Environ. Sci.: Water Res. Technol. (2019), https://doi.org/10.1039/c9ew00835g.
[46] M.R. Cerón, et al., Cation selectivity in capacitive deionization: elucidating the role of pore size, electrode potential, and ion dehydration, ACS Appl. Mater. Interfaces 12 (2020) 42644–42652.
[47] H. Imai, T. Terada, T. Miura, S. Yamabi, Self-organized formation of porous aragonite with silicate, J. Cryst. Growth 244 (2002) 200–205.
[48] M. Ni, B.D. Ratner, Differentiating calcium carbonate polymorphs by surface analysis techniques - an XPS and TOF-SIMS study, Surf. Interface Anal. 40 (2008) 1356–1361.
[49] D. Chakrabarty, S. Mahapatra, Aragonite crystals with unconventional morphologies, J. Mater. Chem. 9 (1999) 2953–2957.
[50] K.M. Barcelos, K.S.G.C. Oliveira, L.A.M. Ruotolo, Insights on the role of inter-particle porosity and electrode thickness on capacitive deionization performance for desalination, Desalination 492 (2020) 114594.
[51] Yan, T., Xu, B., Zhang, J., Shi, L. & Zhang, D. RSC Advances enhanced capacitive deionization †. 2490–2497 (2018). doi:https://doi.org/10.1039/c7ra10443j.
[52] A.C. Arulrajan, J.E. Dykstra, A. Van Der Wal, S. Porada, Unravelling pH changes in electrochemical desalination with capacitive deionization, Environ. Sci. Technol. 55 (2021) 14165–14172.
[53] Jae-Hwan Choi, H.-S. K., Scale formation by electrode reactions in capacitive deionization and its effects on desalination performance, Appl. Chem. Eng. 27 (2016) 74–79.
[54] J.H. Bang, et al., Specific surface area and particle size of calcium carbonate precipitated by carbon dioxide microbubbles, Chem. Eng. J. 198–199 (2012) 254–260.
[55] J. Shim, et al., Influence of natural organic matter on membrane capacitive deionization performance, Chemosphere 264 (2021) 128519.
[56] J.J. Lado, et al., Continuous cycling of an asymmetric capacitive deionization system: an evaluation of the electrode performance and stability, J. Environ. Chem. Eng. 3 (2015) 2358–2367.
[57] N.E. Holubowitch, A. Omosebi, X. Gao, J. Landon, K. Liu, Membrane-free electrochemical deoxygenation of aqueous solutions using symmetric activated carbon electrodes in flow-through cells, Electrochim. Acta 297 (2019) 163–172.
[58] A. Omosebi, X. Gao, J. Landon, K. Liu, Asymmetric electrode configuration for enhanced membrane capacitive deionization, ACS Appl. Mater. Interfaces 6 (2014) 12640–12649.
[59] R. Berenguer, E. Morallón, Oxidation of Different Microporous Carbons by Chemical and Electrochemical Methods. 6 (2019) 1–14.
[60] Ros, T. G., Dillen, A. J. Van, Geus, J. W. & Koningsberger, D. C. Surface Oxidation of Carbon Nanofibres. 1151–1162 (2002).
[61] J. Jaramillo, P. Modesto, V. Gómez-serrano, Oxidation of activated carbon by dry and wet methods surface chemistry and textural modi fi cations, Fuel Process. Technol. 91 (2010) 1768–1775.
[62] G. Huang, Q. Geng, W. Kang, Y. Liu, Y. Li, B. Xing, C. Zhang, Hierarchical porous carbon with optimized mesopore structure and nitrogen doping for supercapacitor electrodes, Microporous Mesoporous Mater. 288 (2019) 109576.
[63] A. Serrano Mora, A.P. Soleymani, J. Jankovic, D.P. Wilkinson, M. Mohseni, Influence of dissolved organic matter and iron on the anodic capacitance and potential at the point of zero charge of activated carbon electrodes used in capacitive deionization, Desalination 532 (2022) 115707.
[64] B.A. Mei, O. Munteshari, J. Lau, B. Dunn, L. Pilon, Physical interpretations of Nyquist plots for EDLC electrodes and devices, J. Phys. Chem. C 122 (2018) 194–206.
[65] M. Lenz, J. Zabel, M. Franzreb, New approach for investigating diffusion kinetics within capacitive deionization electrodes using electrochemical impedance spectroscopy, Front. Mater. 7 (2020) 1–12.
[66] Y.R. Nian, H. Teng, Influence of surface oxides on the impedance behavior of carbon-based electrochemical capacitors, J. Electroanal. Chem. 540 (2003) 119–127.
[67] M. Arulepp, et al., Influence of the solvent properties on the characteristics of a double layer capacitor, J. Power Sources 133 (2004) 320–328.
[68] M. Li, H.G. Park, Pseudocapacitive coating for effective capacitive deionization, ACS Appl. Mater. Interfaces 10 (2018) 2442–2450.
[69] B.H. Min, J.H. Choi, K.Y. Jung, Improvement of capacitive deionization performance via using a Tiron-grafted TiO2 nanoparticle layer on porous carbon electrode, Korean J. Chem. Eng. 35 (2018) 272–282.
[70] D. He, C.E. Wong, W. Tang, P. Kovalsky, T. David Waite, Faradaic reactions in water desalination by batch-mode capacitive deionization, Environ. Sci. Technol. Lett. 3 (2016) 222–226.
[71] J. Marín-Cruz, R. Cabrera-Sierra, M.A. Pech-Canul, I. González, Characterization of different allotropic forms of calcium carbonate scales on carbon steel by electrochemical impedance spectroscopy, J. Appl. Electrochem. 34 (2004) 337–343.
[72] Z. Zuo, et al., Effect of scale inhibitors on the structure and morphology of CaCO3 crystal electrochemically deposited on TA1 alloy, J. Colloid Interface Sci. 562 (2020) 558–566.
[73] Q. Cheng, et al., Graphene and nanostructured MnO2 composite electrodes for super- capacitors, Carbon N. Y. 49 (2011) 2917–2925.